

Time-gated FRET nanoassemblies for rapid and sensitive intra- and extracellular fluorescence imaging

Hamid Samareh Afsari,¹ Marcelina Cardoso Dos Santos,² Stina Lindén,² Ting Chen,¹ Xue Qiu,² Paul M. P. van Bergen en Henegouwen,³ Travis L. Jennings,⁴ Kimihiro Susumu,^{5,6} Igor L. Medintz,⁷ Niko Hildebrandt,^{2*} Lawrence W. Miller^{1*}

2016 © The Authors, some rights reserved; exclusive licensee American Association for the Advancement of Science. Distributed under a Creative Commons Attribution NonCommercial License 4.0 (CC BY-NC). 10.1126/sciadv.1600265

Time-gated Förster resonance energy transfer (FRET) using the unique material combination of long-lifetime terbium complexes (Tb) and semiconductor quantum dots (QDs) provides many advantages for highly sensitive and multiplexed biosensing. Although time-gated detection can efficiently suppress sample autofluorescence and background fluorescence from directly excited FRET acceptors, Tb-to-QD FRET has rarely been exploited for biomolecular imaging. We demonstrate Tb-to-QD time-gated FRET nanoassemblies that can be applied for intra- and extracellular imaging. Immunostaining of different epitopes of the epidermal growth factor receptor (EGFR) with Tb- and QD-conjugated antibodies and nanobodies allowed for efficient Tb-to-QD FRET on A431 cell membranes. The broad usability of Tb-to-QD FRET was further demonstrated by intracellular Tb-to-QD FRET and Tb-to-QD-to-dye FRET using microinjection as well as cell-penetrating peptide-mediated endocytosis with HeLa cells. Effective brightness enhancement by FRET from several Tb to the same QD, the use of low nanomolar concentrations, and the quick and sensitive detection void of FRET acceptor background fluorescence are important advantages for advanced intra- and extracellular imaging of biomolecular interactions.

INTRODUCTION

Fluorescent biosensors are essential tools that make it possible to dynamically visualize molecular interactions, second-messenger concentrations, and other biologically relevant species and processes in living cells (1, 2). Microscopic imaging of Förster resonance energy transfer (FRET) between two proximal fluorophores, usually fluorescent proteins (FPs), is the most common strategy for engineering biosensors (3). FRET is a nonradiative transfer of energy from an excited donor fluorophore to a nearby acceptor, whose absorption spectrum must overlap with the photoluminescence (PL) spectrum of the donor (spectral overlap). FRET can be detected as a decrease in the PL intensity or lifetime of the donor or as an increase in the PL intensity of the acceptor, if the acceptor is fluorescent (4). Because FRET is highly sensitive to changes in distance over a scale of ca. 1 to 20 nm, it is particularly useful for measuring changes in the level of interaction between two proteins or conformational changes within a single protein. Although FPs are the most widely used fluorescent labels for cell-based studies, their broad and overlapping spectra necessitate acquisition and processing of two or three images per frame, resulting in lower FRET signal-to-noise ratio and temporal resolution (5, 6). Moreover, it is very difficult to accurately measure signals from two or more colocalized FRET pairs (2, 7, 8).

Unlike FPs or other conventional fluorescent materials, luminescent lanthanide (Ln) complexes have millisecond-scale excited-state life-

times and multiple, narrow-line emission bands that span the visible spectrum (9). Brightly luminescent Tb(III) and Eu(III) complexes offer distinct advantages as FRET donors for biosensor design and imaging (10–13). First, the narrow emission bands can be easily filtered from sensitized acceptor emission signals. Second, long-lived, Ln-sensitized acceptor emission can be separated from short-lived scattering, directly excited acceptor fluorescence, and autofluorescence background by time gating, where the detector starts collecting light after a brief delay that follows pulsed excitation. A third benefit of Ln-based FRET is that it affords the possibility of multiplexed detection or imaging where, for example, Tb(III) can sensitize emission of two or more differentially colored acceptors (11). All of these features have been leveraged extensively to develop biosensors for both solution-phase assays using commercial plate reader instrumentation (14–16) and biomolecular imaging using a variety of custom-built, time-gated (TG) luminescence microscopes (17–21).

The application of quantum dots (QDs) as acceptors can further improve Ln-based FRET in multiple ways, including (i) distance range (large spectral overlap integrals), (ii) sensitivity (high QD brightness and sequential FRET from several Ln complexes to the same QD), (iii) multiplexing (spectrally broad absorption and narrow emission), and (iv) versatility (attachment of several biomolecules and fluorophores to the QD surface) (11, 22–30). Despite all these exceptional FRET properties and the various multiplexed and sensitive biosensing applications already prototyped with this functional materials combination, only two studies have demonstrated initial proof of concept for Ln-to-QD FRET imaging by using biotin-streptavidin interaction (20, 23). Whereas the first one simply imaged the FRET process on microbeads, the second study applied Ln-to-QD FRET for cellular imaging using a Lumi4-Tb complex (Tb) as donor and two different QDs as acceptors. However, only one QD color was used at a time, and the Tb donor and QD acceptor were attached to the same substrate for a SNAP-tag that

¹Department of Chemistry, University of Illinois at Chicago, 845 West Taylor Street, Chicago, IL 60607–7061, USA. ²NanoBioPhotonics (www.nanofret.com), Institut d'Electronique Fondamentale, Université Paris-Saclay, Université Paris-Sud, CNRS, 91405 Orsay Cedex, France. ³Cell Biology, Department of Biology, Science Faculty, Utrecht University, 3584 CH Utrecht, Netherlands. ⁴Affymetrix Inc., 10255 Science Center Drive, San Diego, CA 92121, USA. ⁵Optical Sciences Division, Code 5611, U.S. Naval Research Laboratory, Washington, DC 20375, USA. ⁶Sotera Defense Solutions, Columbia, MD 21046, USA. ⁷Center for Bio/Molecular Science and Engineering, Code 6900, U.S. Naval Research Laboratory, Washington, DC 20375, USA. *Corresponding author. Email: niko.hildebrandt@u-psud.fr (N.H.); lwm2006@uic.edu (L.W.M.)

was expressed on an extracellular dopamine receptor (20). Therefore, several functional aspects with paramount importance for widely applicable Ln-to-QD intra- and extracellular imaging are still missing: (i) the use of QD- and Tb-antibody conjugates (because immunostaining is one of the most frequently applied technique for fluorescence imaging); (ii) specificity of these antibody conjugates to different receptors or different epitopes on the same receptor (to demonstrate the applicability of Ln-to-QD FRET between two different biological entities); (iii) intracellular delivery and Ln-to-QD FRET imaging in the cytosol and subcellular compartments (to demonstrate Ln-to-QD FRET applicability inside cells under different environmental conditions); and (iv) multi-step Ln-to-QD-to-dye FRET imaging (to demonstrate the multiplexed imaging potential on a single QD).

Here, we demonstrate that all these important requirements can be fulfilled and that the many advantages of Tb-QD FRET nanoassemblies can be exploited for a broad range of biomolecular imaging applications on and in cells. We have investigated several different extra- and intracellular Tb-to-QD FRET systems on live and fixed cells using two different TG PL microscope setups. For cell surface studies, two different therapeutic antibodies, cetuximab and matuzumab (Merck), that recognize different epitopes on the epidermal growth factor receptor (EGFR) were conjugated to Tb and QDs, respectively. The conjugates bound to EGFR on the surface of cultured A431 cells, as indicated by a robust, intramolecular Tb-to-QD FRET signal. Similar results were found when Tb and QD were conjugated to different single-domain antibodies against different EGFR epitopes. For intracellular imaging in HeLa cells, Tb-functionalized peptides (Tb-pep) and cell-penetrating peptides (CPPs) were prepared as described (31) and attached to the QD surfaces via polyhistidine self-assembly with varying valencies of Tb-pep and CPP (32). QD-Tb-pep conjugates were microinjected, and QD-Tb-pep-CPP conjugates were endocytosed. Tb-to-QD FRET signals were visualized and quantified in the cytoplasm and the endosomes/lysosomes, respectively. Cytoplasmic signals from QD-Tb-pep assemblies could be detected when the estimated cellular Tb concentration was only 50 nM, highlighting the PL signal amplification that occurs when multiple,

long-lifetime Tb donors are paired with a single QD acceptor. Finally, we demonstrate intracellular TG imaging of a three-way FRET relay assembly, in which a single QD accepts energy from multiple Tb donors, and the excited QD subsequently transfers energy to multiple downstream dye acceptors. Together, these results show that carefully designed Ln-QD FRET nanoassemblies have considerable potential for sensitive and versatile biosensing when applied to fixed and live cell imaging.

RESULTS AND DISCUSSION

We used three approaches to show the broad applicability of the Tb-QD FRET system for imaging biomolecular interactions on the cellular and subcellular level (Fig. 1). A proof of concept for detecting protein-protein interactions by Tb-to-QD FRET was established by immunostaining of different epitopes of EGFR on cellular membranes. Intracellular FRET biosensing capability was demonstrated by microinjected Tb-to-QD FRET and Tb-to-QD-to-dye FRET relay nanoassemblies and cellular uptake by Tb-QD FRET pairs that were cofunctionalized with CPPs.

Extracellular Tb-to-QD FRET using immunostaining

To demonstrate the feasibility of extracellular Tb-to-QD FRET biosensing by immunostaining with different kinds of antibodies, we used cetuximab and matuzumab antibodies and EgA1 and EgB4 single-domain V_HH (variable domain of heavy chain) antibodies (nanobodies) that recognize different epitopes of EGFR (33, 34). eBioscience eFluor 650NC QDs emitting at 650 nm (QD650) were surface-functionalized with cetuximab and EgB4, and ultraviolet-visible (UV-Vis) absorption spectroscopy revealed that the average degrees of labeling (DOLs) were approximately 6.8 cetuximab per QD650 and 18.1 EgB4 per QD650. Matuzumab and EgA1 were reacted with *N*-hydroxysuccinimide (NHS)-functionalized Lumi4-Tb (Tb), and the DOLs were ca. 4.1 Tb per matuzumab and 2.2 Tb per EgA1. We then incubated live A431 cells

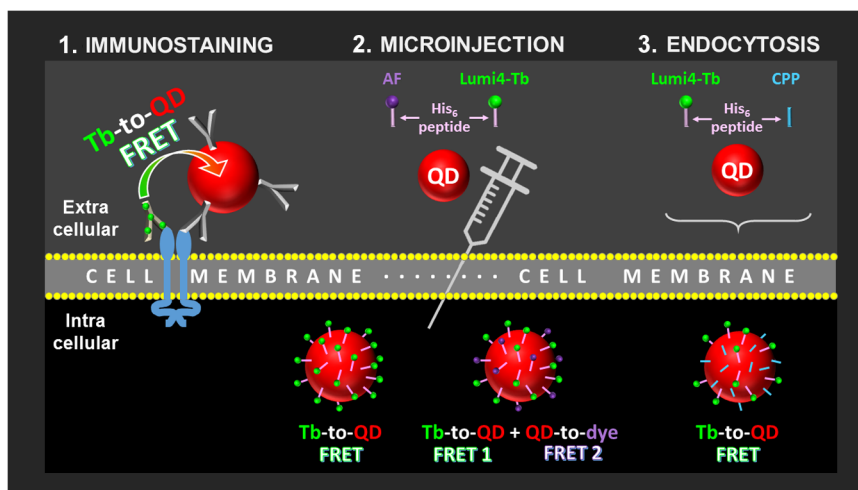


Fig. 1. Schematic presentation of the FRET imaging approaches used in this study. (1) Extracellular FRET between Tb- and QD-functionalized antibodies that bind to different epitopes of EGFR on the cell membrane. (2) Intracellular (cytosol) FRET from Tb-to-QD and FRET relays from Tb-to-QD-to-dye using microinjected QDs conjugated with Alexa Fluor 647 (AF) and Lumi4-Tb peptides via hexahistidine (His₆) self-assembly. (3) Intracellular (endosomes/lysosomes) FRET from Tb-to-QD using CPP-mediated endocytosis of QDs conjugated with Lumi4-Tb peptides via hexahistidine self-assembly.

in culture medium that contained QD650-cetuximab (9.5 nM) and matuzumab-Tb (100 nM) for 30 min, washed the cells, and mounted them immediately on the microscope slide for imaging. TG imaging revealed robust, long-lived PL signals in both the Tb (494-nm) and the QD (650-nm) detection channels (Fig. 2A). Similar results were seen when A431 cells were co-incubated with the nanobody conjugates QD650-EgB4 and EgA1-Tb (Fig. 2B). By contrast, hardly any appreciable long-lived TG signal was detectable in the QD channel when cells were incubated with QD conjugates or Tb conjugates alone (Fig. 2, C and D). Moreover, Tb-mediated FRET was undetectable on A431 cells colabeled with matuzumab-Tb and human epidermal growth factor receptor 2 (HER2)-specific antibodies conjugated to a QD (fig. S1), although TG Tb PL and steady-state (SS) QD PL could both be detected. Thus, by eliminating short-lived, nonspecific signals, intermolecular FRET between both two different immunoglobulin G antibodies and two different single-domain antibodies could be clearly visualized, which demonstrated the applicability of the Tb-QD FRET pair for imaging protein-protein interactions on cell membranes. Moreover, this FRET system can also be used for a homogeneous (no separation or washing steps) imaging of proteins that express on cellular membranes, similar to FRET in vitro assays (28, 35). This application would be particularly interesting for live cell imaging or multiplexing.

Intracellular Tb-to-QD FRET in the cytosol using microinjection

The large difference in excited-state lifetimes of the Tb donor (milliseconds) and the QD acceptor (nanoseconds) permits multiple sequential FRET excitations of a single QD by several Tb donors (11). The

effective brightness, or rate of photon emission, increases along with the number of surface-bound Tb donors, in a manner that is independent of FRET efficiency and excitation light flux (assuming that light intensity is high enough to excite several Tb donors at once). Such a brightness enhancement has also been observed in solution-phase Tb-to-QD FRET immunoassays (28). To demonstrate this brightness enhancement of FRET-sensitized QDs in an imaging context, we attached Tb-pep via hexahistidine (His₆)-mediated self-assembly at controllable valencies (x Tb per QD) to the Zn-rich surface of 625-nm emitting QDs (QD625) functionalized with CL4 compact ligands (36). QDs prepared in this manner have already been proven to be quite robust and tolerate complex cellular environments (37, 38). The Tb _{x} -QD nanoassemblies (0.5 μ M) were then microinjected into the cytoplasm of live HeLa cells. SS QD PL and TG Tb and QD PL were clearly visible and spread over the entire cytoplasm (Fig. 3A). The TG Tb PL signal seen in the nucleus (Fig. 3A, middle) can be attributed to the presence of free Tb peptide, which is small enough to diffuse through nuclear pores. We observed an increase in the ratio of the TG Tb-to-QD FRET to SS QD PL signals with increasing x (Fig. 3B), which demonstrates the brightness enhancement effect mentioned above. A similar trend was seen if the QD concentration in the injection solution was increased to 0.9 μ M (fig. S2). At a Tb/QD valency of ca. 25, the FRET ratio increase began to level off, suggesting a beginning saturation of the QD surface. For valencies of $x \geq 40$, precipitation occurred at both QD concentrations. We attribute this to the paucity of hydrophilic residues in the peptide along with the nature of the Tb complex itself, which cumulatively destabilize the QD's colloidal stability at high localized concentrations.

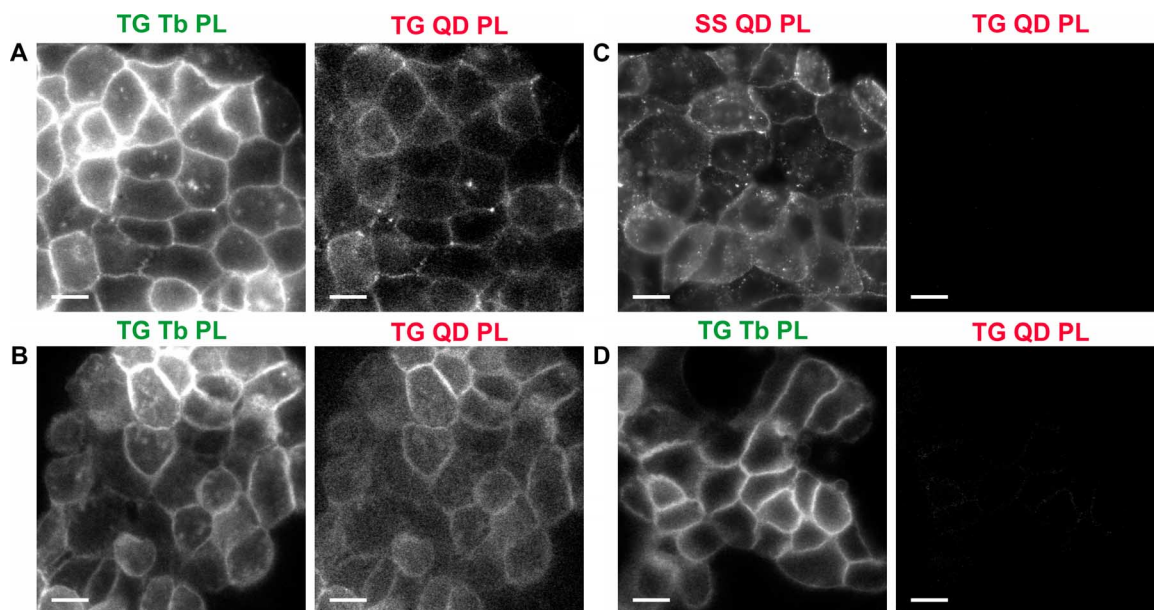


Fig. 2. Extracellular Tb-to-QD FRET using immunostaining of EGFR. (A and B) Tb-to-QD FRET detected on A431 cells with QD- and Tb-conjugated antibodies (A) and nanobodies (B). For both immunostaining approaches, the time-gated Tb (TG Tb PL) and QD (TG QD PL) channels reveal bright PL signals originating mainly from the cell membranes. (C and D) In contrast, staining with only QD-antibodies (C) or only Tb-antibodies (D) does not result in TG PL in the QD channel (TG QD PL, right), and only the pure QD SS PL (C, SS QD PL, left) or the pure TG Tb PL (D, left) become visible. Excitation and emission wavelengths for the different detection channels were as follows: $\lambda_{\text{ex}} = 365$ nm and $\lambda_{\text{em}} = 494 \pm 10$ nm for TG Tb PL, $\lambda_{\text{ex}} = 365$ nm and $\lambda_{\text{em}} = 655 \pm 20$ nm for TG QD PL, and $\lambda_{\text{ex}} = 545 \pm 15$ nm and $\lambda_{\text{em}} = 610 \pm 35$ nm for SS QD PL. For TG images, the number of integrations was 220 and 110 for the TG Tb PL and TG QD PL channels, respectively. Tb-to-QD FRET channel images (TG QD PL) were corrected for spectral crosstalk, and each TG QD PL channel image in this figure is presented at identical contrast. Scale bars, 20 μ m.

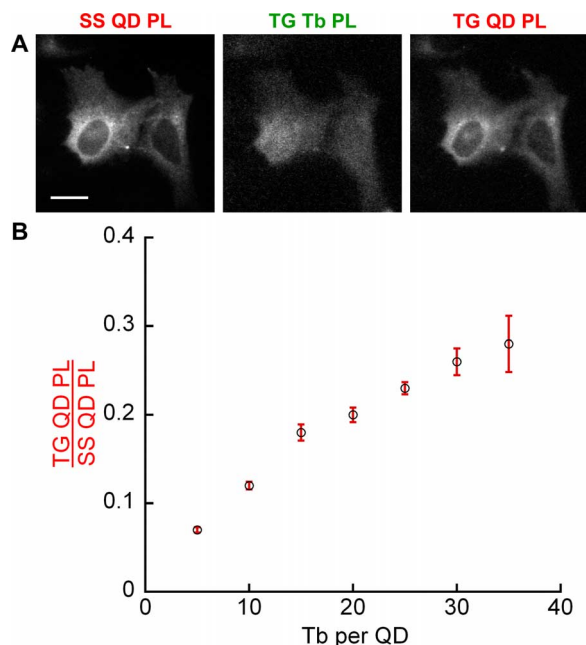


Fig. 3. Intracellular Tb-to-QD FRET increase with increasing Tb per QD valencies. (A) PL images showing cells after injection with Tb_{15} -QD solution (QD concentration, $0.5 \mu\text{M}$). Excitation and emission wavelengths for the different detection channels were as follows: $\lambda_{\text{ex}} = 545 \pm 15 \text{ nm}$ and $\lambda_{\text{em}} = 610 \pm 35 \text{ nm}$ for SS QD (SS QD PL), $\lambda_{\text{ex}} = 365 \text{ nm}$ and $\lambda_{\text{em}} = 494 \pm 10 \text{ nm}$ for TG Tb (TG Tb PL), and $\lambda_{\text{ex}} = 365 \text{ nm}$ and $\lambda_{\text{em}} = 605 \pm 8 \text{ nm}$ for TG Tb-to-QD FRET (TG QD PL). For TG images, the number of integrations was 660. TG QD PL channel images were corrected for spectral crosstalk. Scale bar, $20 \mu\text{m}$. (B) Ratio of spectral crosstalk-corrected TG QD PL signal to SS QD PL signal plotted as a function of Tb per QD molar ratio in the injection solution. The FRET ratio clearly increases with the number of Tb on the QD surface, indicating QD-FRET sensitization by multiple Tbs. PL intensities of TG and SS QD channels were taken from several regions of interest (ROIs) of ≥ 10 cells under each condition. Error bars, SEM.

Another important aspect for a broad applicability of Ln-to-QD FRET concerns the overall abundance of Tb_x -QD assemblies that were imaged within the cytoplasm of the live cells. To analyze this, we used a recently developed method, in which we calibrated our TG microscope to relate pixel gray value under a given set of illumination conditions to the absolute concentration of Tb molecules in the cytoplasm (39). By injecting Tb solutions of varied concentrations into HeLa cells and applying the previously determined calibration curve, the microinjection system was calibrated so that cytoplasmic solute concentration could be estimated from the solute concentration in the injection solution (fig. S3). The results of this calibration showed that the concentration of a solute in the cytoplasm was about 2% of that in the injection solution. Taking into account the injection solution concentrations of $0.5 \mu\text{M}$, we were able to detect Tb-to-QD FRET signals when the cytoplasmic concentration of Tb-QD assemblies was only 10 nM (about 10^4 copies per cell), with valencies down to 5 Tb (50 nM) per QD (Fig. 3B), and Tb_{15} -QD assemblies could be easily visualized at that level (Fig. 3A). By comparison, the limiting concentration for microscopically detecting green fluorescent protein fluorescence in the cytoplasm is about 200 nM (40), and we previously established a low-micromolar limit for TG detection of cytoplasmic Tb using the same imaging setup (39). The results presented

here clearly show that the large difference in the excited-state lifetimes of Tb donors and QD acceptors can be leveraged to effectively amplify Tb-mediated FRET signals, resulting in a 100-fold increase in TG detection sensitivity. Such Tb-QD FRET systems were already used for multiplexed detection of microRNA (30), DNA (27), and protease activity (41). The demonstration of bright intracellular Tb-to-QD FRET is therefore a highly important step toward the application of this FRET pair to investigating nucleic acids and enzyme kinetics inside cells.

Intracellular Tb-to-QD-to-dye FRET relays in the cytosol using microinjection

To demonstrate that QDs can also be used as intracellular FRET relays, in which the QD acts as both FRET acceptor and donor, we co-assembled QDs with Tb donor- and dye acceptor (AF)-labeled peptides to observe Tb-to-QD-to-AF FRET in live cells. The AF dye was spectrally selected to be an appropriate downstream acceptor to the QD. QD625 ($2 \mu\text{M}$) was incubated with a 20-fold molar excess of Tb-pep ($40 \mu\text{M}$) for about 1 hour, after which AF peptides were added at various concentrations between 5 and $20 \mu\text{M}$ (with y being the number of AF per QD). The Tb_{20} -QD-AF $_y$ assemblies were injected into HeLa cells and imaged in both SS and TG modes. As shown in Fig. 4, both TG Tb and QD (Tb-to-QD FRET) PL signals were clearly observable for all Tb_{20} -QD-AF $_y$ combinations, whereas TG AF (Tb-to-QD-to-AF FRET) PL only became apparent in assemblies that contained AF ($y \geq 5$). A quantitative analysis (Fig. 4B) showed that increasing valencies of AF on the QD (at a fixed Tb valency of $x = 20$) led to a weak decrease in the ratio of TG QD PL to SS QD PL (because TG QD PL decreases slightly more strongly than SS QD PL) and a strong increase in the ratio of TG AF PL to SS QD PL. This significant intensity increase provided further strong evidence that the energy is passed from Tb to AF via QD and of the functionality of the QD-mediated FRET relay. It should be noted that direct Tb-to-AF FRET cannot be excluded because the Tb PL and AF absorption show some relevant spectral overlap. However, as demonstrated for the same system applied to in vitro assays (27), the significant differences in Förster distances [$R_0(\text{Tb-to-QD}) = 10.1 \text{ nm}$, $R_0(\text{QD-to-AF}) = 7.5 \text{ nm}$, and $R_0(\text{Tb-to-AF}) = 5.7 \text{ nm}$] make Tb-to-AF FRET 30- and 5-fold slower than Tb-to-QD and QD-to-AF FRET, respectively. Therefore, a direct Tb-to-AF FRET would only provide a minor contribution to the complete FRET relay system. The capability of TG imaging of Tb-to-QD-to-dye FRET relays presents an important proof of principle of using these multiple FRET step systems for intracellular biosensing applications, such as multiplexed analysis of enzyme kinetics (41), DNA hybridization (27), or molecular logic devices (42, 43).

Intracellular Tb-to-QD FRET in endosomes/lysosomes using CPP-mediated endocytosis

To investigate another cellular delivery method that is less technically demanding than microinjection, we used CPPs that were also self-assembled via His $_6$ to the QD625 surface functionalized with a polyethylene glycol (PEG)-methoxy ligand in this case (36, 44). Cellular delivery of QDs via CPP-mediated endocytosis has been demonstrated many times before (45, 46), and this particular CPP (R9GGLAAIbSGWKH6) was shown to deliver QDs mainly in endosomes and, later, lysosomes (47). It is well known that in eukaryotic cells, endosomes typically undergo constitutive acidification as they mature with time (48). This can, in turn, potentially affect the emissive and FRET properties of fluorophores located within the endosomes (49). Indeed, pH-sensitive fluorescent dyes are used for sensing purposes in these and similar

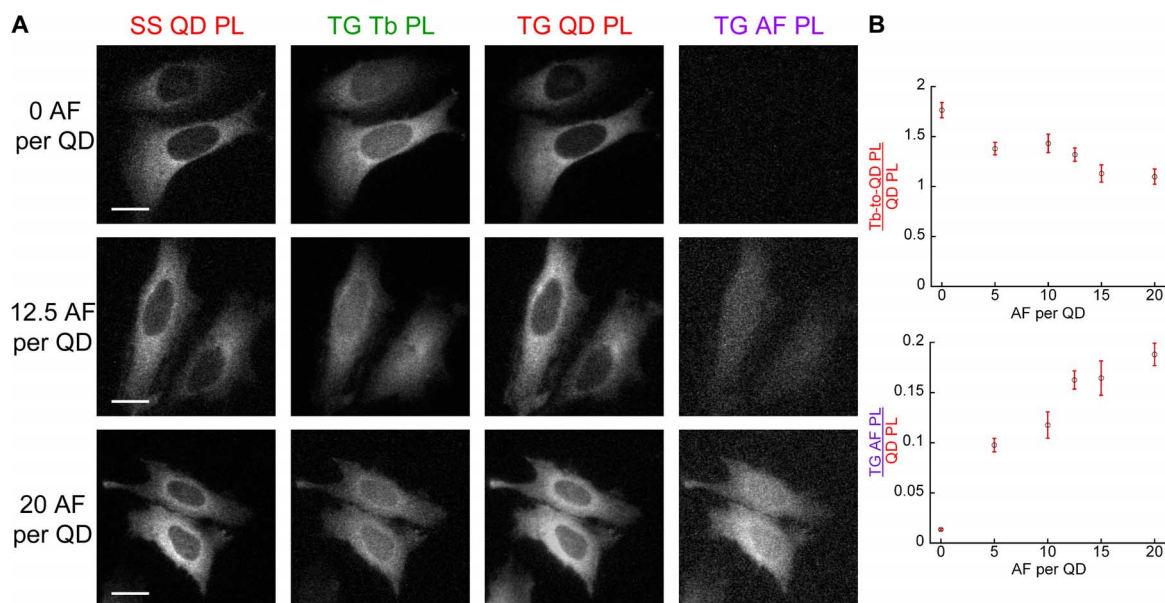


Fig. 4. Intracellular Tb-to-QD FRET and Tb-to-QD-to-dye FRET relays after microinjection into live HeLa cells. (A) PL images showing cells after injection with Tb_{20} -QD-AF $_y$ nanoassemblies with AF valencies (y) of 0, 12.5, or 20 (from top to bottom). Excitation and emission wavelengths for the different detection channels were as follows: $\lambda_{ex} = 545 \pm 15$ nm and $\lambda_{em} = 605 \pm 8$ nm for SS QD PL, $\lambda_{ex} = 365$ nm and $\lambda_{em} = 494 \pm 10$ nm for TG Tb (TG Tb PL), $\lambda_{ex} = 365$ nm and $\lambda_{em} = 605 \pm 8$ nm for TG Tb-to-QD FRET (TG QD PL), and $\lambda_{ex} = 365$ nm and $\lambda_{em} = 710 \pm 20$ nm for TG Tb-to-QD-to-AF FRET (TG AF PL). For TG images, the number of integrations was 660. TG QD PL channel images were corrected for spectral crosstalk. Scale bars, 20 μ m. **(B)** Ratio of spectral crosstalk-corrected TG QD PL signal to SS QD PL signal (top) and TG AF PL signal to SS QD PL signal (bottom) plotted as a function of AF per QD molar ratio in injection solution. The ratio of TG QD PL to SS QD PL decreases slightly as the number of AF on the QD surface is increased, whereas the TG AF PL-to-SS QD PL ratio increases substantially. This indicates a Tb-to-AF FRET relayed by the central QD. PL intensities of Tb-to-QD FRET, Tb-to-QD-to-AF FRET, and QD channels were taken from several ROIs of ≥ 10 cells for each condition. Error bars, SEM.

scenarios. There are also examples of pH-sensitive QDs being used for these purposes, although they consist of CdTe cores without a protective overcoating shell (50). Such sensitivities can also have marked effects on FRET efficiency by altering the photophysical properties of the donor/acceptor materials. Considering these points, it is important to note that the QD materials along with the AF dye that we used are stable and unaffected by the expected range of pH changes encountered here (36, 51). In a similar vein, the intracellular integrity of the Tb within the Tb-chelate may also be a potential issue (52). However, the structure of the isophthalamide-type ligand that chelates the Tb ion is designed to hold the atom with very high affinity (53). Given this, in conjunction with the lack of any observed significant changes in FRET efficiency over the lifetime of the experiments, we conclude that intracellular pH and molecular degradation are not pertinent issues here.

To first test different uptake conditions, we compared various QD incubation concentrations and valencies of CPPs per QD before the addition of Tb-pep. For a fixed valency of 25 CPPs per QD, endocytosis could be clearly observed at QD concentrations of 25 and 100 nM, whereas the same concentrations of QDs without CPPs did not lead to any significant cellular uptake (fig. S4). Because the signal-to-noise ratios were similar for both concentrations, we decided to work with the lower concentration of 25 nM for testing different valencies of CPPs per QD. PL images showed no visible cellular uptake for valencies ≤ 10 , but 15 and 25 CPPs per QD led to clearly visible endocytosis of the QDs with the typical pointed PL spots inside the cells, indicating that the QDs mainly remain in endosomes or lysosomes (fig. S5) and are not or only partly released into the cytosol. Although 15 CPPs per QD al-

ready provided a sufficient signal-to-noise ratio for imaging, it could be more than doubled for 25 CPPs under the same imaging conditions, showing that the cellular uptake was more than twice as efficient when using 25 instead of 15 CPPs. We therefore decided to use a fixed valency of 25 CPPs per QD for the following coassembly experiments of CPPs and Tb-pep on the same QD. Tb-pep at 12.5-, 25-, 35-, and 45-fold the QD concentration were incubated with the CPP₂₅-QD assemblies, and TG images were recorded in both the Tb and QD channels (Fig. 5). The QD625 sample has a hard diameter of ~ 9.3 nm, which suggests that it should be able to accommodate a surface display of ~ 60 peptides; however, this does not predict their effects on colloidal stability (54, 55). For the CPP₂₅-QD-Tb_{12.5} nanoassembly, no specific TG PL signal, which would be easily distinguishable from the background noise, could be detected either in the Tb or in the QD channel. At valencies of ≥ 25 , the intracellular PL resulting from Tb PL and Tb-sensitized QD PL became clearly visible. For all three systems, the Tb-to-QD FRET signals are brighter than the Tb donor signals, which confirms the brightness enhancement effect caused by FRET from multiple Tbs to the QD (vide supra). For the CPP₂₅-QD-Tb₂₅ assembly, the intracellular labeling appears as the most homogeneous (in particular in the Tb-to-QD FRET channel), whereas intracellular precipitation occurs at higher Tb valencies. This confirms the microinjection experiments, in which a precipitation was found at high peptide-per-QD ratios (vide supra). Another interesting result concerns the images in the Tb channel. At a valency of 25 Tb per QD, FRET to the QD is very efficient and the TG QD PL is brighter than the FRET-quenched Tb PL, which is only slightly more intense than the background. At 35 Tb per QD, the Tb-to-QD FRET PL

is still very bright; however, the Tb PL also became significantly stronger than the background PL, which confirms the saturation effect found in the microinjection experiments (Fig. 3B). At even higher valencies (45 Tb per QD), the PL background in the Tb channel becomes significantly stronger, and this is particularly apparent outside the cells. At this valency, a total amount of 60 peptides (25 CPPs and 35 Tb-pep) was mixed with the QDs, and we therefore assign this background increase to some free Tb-pep that could not bind effectively to the already saturated QD surfaces.

Taking into account the previous coassembly and concentration-dependent experiments, as well as the microinjection results, we performed further CPP-QD-Tb intracellular TG FRET imaging experiments at a larger amount of cells, with QD concentrations of 50 nM and va-

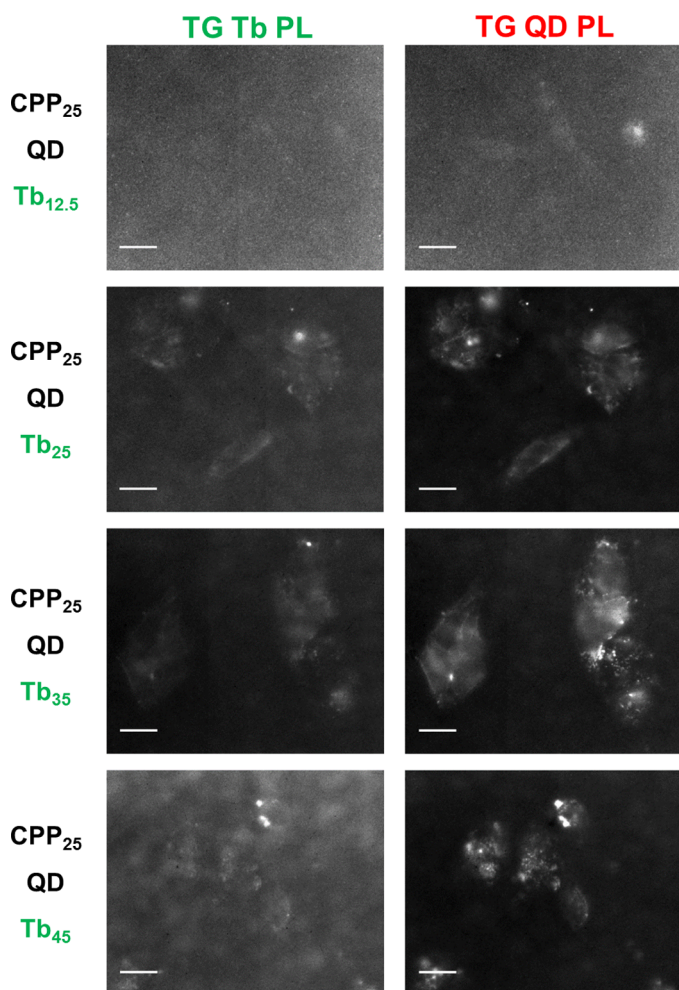


Fig. 5. Intracellular Tb-to-QD FRET after CPP-mediated endocytosis. TG images of different CPP₂₅-QD-Tb_x FRET complexes (with $x = 12.5, 25,$ or 35 from top to bottom) internalized in HeLa cells. All samples were excited at 349 nm with a pulsed (100-Hz) laser. The signals were collected with a 60 \times objective [UPLSAPO, numerical aperture (NA) = 1.35]. Emission wavelengths for the different detection channels were $\lambda_{em} = 542 \pm 20$ nm for TG Tb PL and $\lambda_{em} = 620 \pm 14$ nm for TG Tb-to-QD FRET (TG QD PL). Images were acquired with an intensified charge-coupled device (ICCD) camera, and the gating parameters were fixed at 10 μ s for a gate delay, 2.5 ms for gate width, and 400 gates per exposure. Scale bars, 20 μ m.

lencies of CPP₂₀-QD-Tb₂₀ (Fig. 6) and CPP₄₀-QD-Tb₄₀ (fig. S6). Both nanoassemblies showed obvious cellular uptake in both the TG Tb and QD and the SS QD PL images. However, the CPP₂₀-QD-Tb₂₀ systems provide much brighter and clearer images with less background, as already found in the aforementioned experiments. A quantitative PL intensity analysis using many ROIs from ≥ 20 cells for each of the two different FRET nanoassemblies, and a control setup in which cells were stained only with Tb to account for the spectral crosstalk of Tb PL inside the Tb-to-QD FRET channel, emphasized that both CPP-QD-Tb systems show significant intracellular FRET. Figure 6B shows the average FRET ratios of the Tb-to-QD FRET to Tb channel (the background signal from cell-free regions was subtracted from the ROI signals inside the cells for both channels). The results confirm the significantly higher brightness of the CPP₂₀-QD-Tb₂₀ FRET system, which is about 2.5-fold larger compared to the CPP₄₀-QD-Tb₄₀ assembly. The bigger standard error in the case of the lower valency system is most probably caused by a more heterogeneous distribution of peptides on the QD surfaces and a larger FRET ratio. For 40 peptides, the QD surface is not yet saturated and the valency is expected to be around 40 ± 12 peptides. For an incubation with 80 peptides, the surface of the QD is saturated with peptides, and all free peptides and aggregated nanoassemblies are washed away and do not contribute to the signal. The remaining CPP-QD-Tb

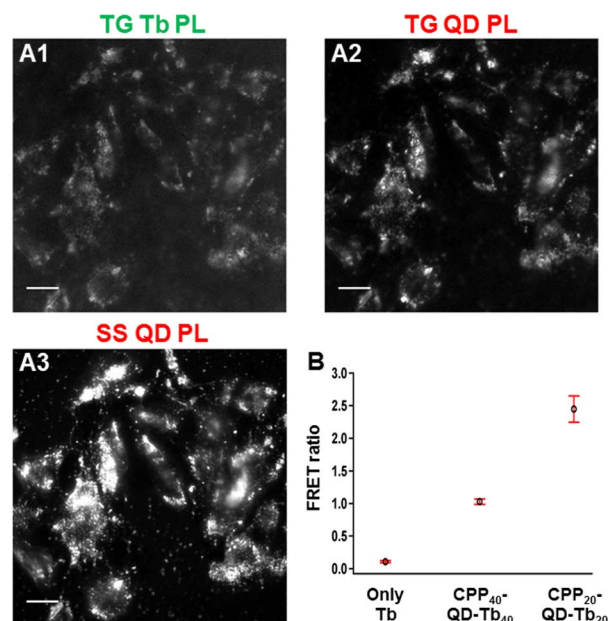


Fig. 6. Influence of different CPP and Tb per QD valency. (A) PL images of CPP₂₀-QD-Tb₂₀ nanoassemblies internalized into HeLa cells. Excitation and emission wavelengths for the different detection channels were as follows: $\lambda_{ex} = 349$ nm and $\lambda_{em} = 542 \pm 20$ nm for TG Tb PL [(A1) TG Tb PL], $\lambda_{ex} = 349$ nm and $\lambda_{em} = 605 \pm 15$ nm for TG Tb-to-QD FRET [(A2) TG QD PL], and $\lambda_{ex} = 494 \pm 20$ nm and $\lambda_{em} = 605 \pm 15$ nm for SS QD [(A3) SS QD PL]. The signals were collected with a 60 \times objective (UplsaPo, NA = 1.35). SS QD images were acquired with a complementary metal-oxide semiconductor (CMOS) camera (acquisition time of 5 ms), and TG Tb PL and TG QD PL images were acquired with an ICCD camera (gating parameters were fixed at 10 μ s for a gate delay, 2.5 ms for gate width, and 800 gates per exposure). Scale bars, 20 μ m. (B) FRET ratios (intensities of TG QD PL to TG Tb PL channels taken from several ROIs of ≥ 20 cells for each system) of pure Tb, CPP₄₀-QD-Tb₄₀, and CPP₂₀-QD-Tb₂₀ nanoassemblies. Error bars, SEM.

nanoassemblies are less intense than in the case of the CPP₂₀-QD-Tb₂₀ system (lower FRET ratio) but also have a less heterogeneous peptide distribution close to the maximum loading capacity, which is expected to be around 50 ± 5 peptides (cf. Fig. 3B). The demonstration of cellular uptake of Tb-QD FRET nanoassemblies by coassembled CPPs is an important step toward the application of this FRET system for intracellular FRET biosensing that cannot use microinjection of single cells. CPP-functionalized QDs have already been used for endocytotic uptake and subsequent delivery into the cytosol with minimal cytotoxic effects (56) and for imaging of spinal cord extension into various cellular systems in a developing avian brain (38). The Tb-QD FRET system may extend this intracellular imaging tool to even more versatile sensing applications.

In conclusion, we have developed several TG Tb-to-QD FRET systems that can be used for intra- and extracellular FRET imaging with very efficient suppression of sample autofluorescence and acceptor fluorescence due to direct excitation, which circumvents the need for separate acquisition of pure acceptor and pure donor PL images as required for conventional FRET imaging experiments. We have demonstrated that Tb-to-QD FRET can be used for extracellular recognition of the membrane receptor EGFR by Tb- and QD-antibody conjugates that recognize different epitopes of EGFR. The application of commercial therapeutic antibodies (cetuximab and matuzumab) and single-domain V_HH antibodies (nanobodies) for successful EGFR FRET detection on live A431 cells showed the wide applicability of the Tb-to-QD FRET pair for immunostaining-based fluorescence imaging. For the demonstration of intracellular Tb-to-QD FRET and Tb-to-QD-to-dye FRET relays, we used Tb-QD-dye nanoassemblies (Tb-pep and dye-peptides self-assembled via His₆ to the QD surfaces) that were microinjected into live HeLa cells. Our experiments showed very efficient FRET and multistep FRET inside the cytosol and a FRET brightness enhancement due to FRET from multiple Tbs to the same QD. This certainly bodes well for future applications that seek to apply the same materials to active sensing configurations. Moreover, we demonstrated that Tb-QD cellular delivery via CPPs (coassembled via His₆ to the QD) is possible, which led to efficient Tb-to-QD FRET (mainly inside endosomes/lysosomes of HeLa cells) again with a FRET brightness enhancement for CPP₂₀-QD-Tb₂₀ nanoassemblies. The large versatility of single and multistep intra- and extracellular FRET, combined with the previously shown possibility of high-order multiplexing with Tb-to-QD-based FRET systems (11), will make Tb-to-QD FRET a very powerful tool for widely applicable intra- and extracellular fluorescence imaging and sensing.

MATERIALS AND METHODS

Materials

A431 cells (CRL-1555) and HeLa cells (CCL-2) were purchased from the American Type Culture Collection. Dulbecco's modified Eagle's medium (DMEM; 10-014-CV), Eagle's minimum essential medium (EMEM; 10-010-CV), phosphate-buffered saline (PBS; 21-014-CV), Dulbecco's PBS (DPBS; 21-030 and 21-031), 0.25% trypsin/0.53 mM EDTA, and 0.25% trypsin/2.21 mM EDTA were purchased from Corning CellGro. MEM nonessential amino acids (11140), DMEM (no phenol red, 21063), and Hepes (15630-080) were purchased from Gibco. Micropipette preparation glass-bottom culture dishes (P50G-0-14-F) were purchased from MafTek Corporation. XenoWorks Microinjection Systems, P-1000 pipette puller, and borosilicate glass tubes (BF100-78-10) were used for microinjections (Sutter Instrument). Cetuximab and matuzumab antibodies

were from Merck. V_HH nanobodies binding to EGFR (EgA1 and EgB4) were produced as described elsewhere (57). Peptides: CPP, R9GGLAAibSGWKH6; Tb-pep, Tbl4-GSGAAAGLS-H6; AF-peptide, AF-CSTRIDEANQAATSLP7SH6). QDs emitting at 625 nm were the same as described previously (36–38, 45). These were made biocompatible by cap exchange with dihydrolipoic acid-modified compact ligand 4 (DHLa-CL4) or DHLa-PEG-methoxy (36, 44). See fig. S7 for ligand structures. Lumi4-Tb reagents were provided by Lumiphore Inc.

QD-antibody conjugation

eFluor 650 Nanocrystal Conjugation Kit–Sulfhydryl Reactive (provided by eBioscience/Affymetrix in lyophilized form) was used for QD conjugations. Before the conjugation, protected sulfhydryl groups (*N*-succinimidyl *S*-acetylthioacetate) were introduced to EgB4 (no sulfhydryl groups available) at 5× molar excess using a SATA kit (no. 26102, Thermo Fisher Scientific). The sulfhydryl groups were deprotected by diacylation according to the manufacturer's protocol. Sulfhydryl-activated EgB4 and cetuximab solutions (in concentration excess compared to the QD solutions) were prepared in 1× PBS and conjugated to QDs according to the manufacturer's instructions. Unbound proteins were separated by washing three to four times in 100-kD molecular weight cutoff (MWCO) spin columns (Millipore), with 100 mM sodium tetraborate buffer (pH 8.3) as the washing buffer. QD concentrations were determined by absorbance measurements using molar absorptivities of $1.1 \times 10^6 \text{ M}^{-1} \text{ cm}^{-1}$ at 641 nm provided by the manufacturer. Antibodies were quantified by absorbance measurements at 280 nm using an extinction coefficient of 1.4 and $2.4 \text{ g}^{-1} \text{ liter}\cdot\text{cm}^{-1}$ for cetuximab and EgB4, respectively. The labeling ratios were determined by linear combination of the respective absorbance values of QDs and antibodies within the QD-antibody conjugates.

Tb-antibody conjugation

Lumi4-Tb-NHS (Tb, provided by Lumiphore in lyophilized form) was used for labeling of matuzumab and EgA1. Tb was dissolved to 8 mM in anhydrous *N,N'*-dimethylformamide and mixed (in concentration excess to the antibodies solutions) with the antibody samples in 100 mM carbonate buffer at pH 9.0. The mixtures were incubated while rotating at 25 rpm (Intelli-Mixer, ELMI) for 2 hours at room temperature. For Tb-conjugate purification, the samples were washed four to six times with 100 mM tris-Cl (pH 7.2) using 50-kD MWCO spin columns for matuzumab and 3-kD MWCO spin columns for EgA1. Tb concentrations were determined by absorbance measurements at 340 nm using a molar absorptivity of $26,000 \text{ M}^{-1} \text{ cm}^{-1}$ as provided by the manufacturer. The labeling ratios were determined by linear combination of the respective absorbance values of Tb and antibodies (1.4 and $2.4 \text{ g}^{-1} \text{ liter}\cdot\text{cm}^{-1}$ at 280 nm for matuzumab and EgA1, respectively) within the Tb-antibody conjugates.

Cell culture

HeLa cells were maintained in DMEM⁺ (DMEM supplemented with 10% FBS, 1× MEM nonessential amino acids, and 15 mM Hepes) at 37°C and 5% CO₂. The cells were passaged with 0.25% trypsin/2.21 mM EDTA. A431 cells were maintained in EMEM⁺ (EMEM supplemented with 10% FBS and 1× MEM nonessential amino acids) at 37°C and 5% CO₂. The cells were passaged with 0.25% trypsin/0.53 mM EDTA.

Cell surface labeling with antibodies/nanobodies

Cells were trypsinized and seeded at 23,000 cells per well in an eight-well chambered cover glass (Nunc, 12-565-470) and incubated at 37°C and

5% CO₂ overnight. The following day, the cells were washed three times with DPBS (+Ca/+Mg), 100 µl of various combinations of QD/Tb-attached antibodies or nanobodies (in DMEM without FBS) was added to different wells, and the cells were incubated for 30 min at 37°C and 5% CO₂. The cells were washed again with DPBS (+Ca/+Mg) and immersed in DMEM without phenol red before imaging.

Self-assembly of peptides on QDs

Tb-pep was mixed with QDs in PBS buffer, and the solution was incubated at room temperature for 2 hours, followed by 16 hours of incubation at 4°C. For measurements of Tb-to-QD-to-AF FRET, AF-peptide was added to the above solution, and the mixture was incubated at room temperature for an additional 1 hour. The solution was filtered before microinjection (0.22 µM).

Microinjection

HeLa cells were grown to 60 to 70% confluency in a glass-bottom dish. A Sutter Instruments P100 pipette puller was used to prepare micropipettes using the following parameters: heat, ramp-40; pull, 90; velocity, 40; time, 100; and pressure, 500. Micropipettes were loaded with the desired solution via capillary action, and the solutions were injected into the cytoplasm using the following microinjector parameters: transfer pressure, 20 hPa; injection width, 0.4 s; and injection pressure, 40 to 60 hPa. For high-concentration solutions (≥ 200 µM) of Lumi4-NH₂ (Tb), injection pressure was raised to 70 to 80 hPa. Before imaging, 100 µl of 1 mM patent blue V solution in DMEM (without phenol red) was added to the cells to quench extracellular luminescence from leakage of Tb-QD conjugates from the microinjection capillary.

TG microscopy with light-emitting diode excitation

Images of cytoplasmic and cell surface Tb-mediated FRET were acquired using a wide-field, TG luminescence microscope that uses a UV light-emitting diode (LED) for pulsed excitation and an ICCD camera for gated detection. The design, operation, and characterization of the microscope system have been described extensively (17, 39, 58, 59). For each TG image acquisition, the signal from multiple excitation/emission events was accumulated on the ICCD sensor and read out at the end of the camera frame. The camera control software enabled summation of multiple frames to yield a single composite TIFF image with a bit depth equal to 1024 multiplied by the number of frames. All images were summations of four frames (bit depth, 4096), and a feature of the camera control software was enabled that removes large variations in signal resulting from ion feedback noise of the intensifier. The UV LED source and the ICCD timing parameters were the same for all of the time-resolved images and data presented here: excitation pulse width, 1500 µs; pulse period, 3000 µs; delay time, 10 µs; intensifier on-time, 1480 µs. Sensitivity was modulated by either varying the frame length (and thus, the number of integrations) or the intensifier gain voltage. All TG images were acquired at an intensifier gain of 889 V, except for images used to calibrate the microinjection system, which were acquired at 833 V.

Image processing

Raw, 12-bit images were imported into National Institutes of Health ImageJ (version 1.47) (60) for all processing operations, including cropping, contrast adjustment, and quantitative analysis. TG images were corrected for flat-field effects as follows. For each channel, 20 dark frames and 20 images of a luminescent Tb complex solution were stacked, converted to 32 bits, and median-filtered (radius 1), and each

stack was averaged. The flat-field average was divided by the mean intensity of its central nine pixels to generate a normalized flat-field image. For each sample image, a median filter (radius 1) was applied and the master dark frame was subtracted. The resulting image was then divided by the normalized, master flat-field image, and the mean value of the detector offset was added back to the image.

TG FRET images were corrected for spectral crosstalk (bleed-through) of the Tb donor signal into the FRET channel. Bleedthrough correction was accomplished by measuring signals from many ROIs (>100) containing Lumi4-NH₂(Tb) probe in both the Tb emission channel (494 ± 10 nm) and the FRET emission channels (605 ± 7 nm, 650 ± 20 nm, and 710 ± 10 nm). The FRET channel signal was plotted as a function of the Tb channel signal, a line was fit to the data, and the slope of that line was taken to be the correction constant. The correction constants for the 605 ± 7-nm and 650 ± 20-nm emission channels were 0.057 and 0.142, respectively. Bleedthrough of Tb signal into the 710 ± 10 nm was negligible. The Tb channel image was multiplied by the appropriate bleedthrough correction constant, and the resulting image was subtracted from the FRET channel image to yield the true FRET image.

Quantitative image analysis

Acceptor-denominated FRET ratios were determined from images of cells injected with Tb-functionalized QDs and QDs functionalized with both Tb and AF dye. Images were visually inspected, and cells that exhibited a diffuse distribution of SS QD fluorescence signal and TG Tb and Tb-to-QD FRET signals throughout the cytoplasm were selected for analysis. Following flat-field correction, the mean gray value of 10 or more background ROIs was measured, and this value was subtracted from the whole image. In the background-subtracted images, the mean gray value within ROIs drawn in the cytoplasm was measured. For each ROI, the TG FRET signal was divided by the SS QD fluorescence signal to yield a ratio, and ratios from multiple ROIs (≥ 10) were averaged.

Microinjection system calibration

The microinjection system was calibrated so that the cytoplasmic concentration of QDs could be related to the QD concentration in the microinjection solution. This was accomplished by imaging cells that were injected with Lumi4-NH₂(Tb) and applying a calibration factor that relates integrated pixel gray value to Tb complex abundance. As previously reported, relation of gray value to Tb complex abundance was accomplished by imaging microbubbles of an aqueous solution of Lumi4-NH₂(Tb) dispersed in mineral oil (39). Integrated pixel gray values within ROIs containing bubbles were plotted as a function of total number of Tb complexes, as determined by microbubble size and solution concentration. By measuring integrated gray counts in ROIs of defined size drawn in the cytoplasm of cells injected with Lumi4-NH₂(Tb), assuming a cell thickness of 5 µm and applying the microbubble calibration factor, it was possible to estimate cytoplasmic Tb concentration. Cells were injected with Lumi4-NH₂(Tb) solutions of varied concentration. Estimated cytoplasmic concentration was determined from ROIs drawn in the cytoplasm and plotted against microinjection solution concentration. From this plot, it was determined that cytoplasmic solute concentration is approximately 2% of its concentration in the injection solution (fig. S3).

Cellular delivery of CPP-QD-Tb nanoassemblies

Lumi4(Tb)-His₆ and QD625 were incubated in DMEM-buffered medium at room temperature for 30 min. Then, CPP was added for an

additional 30 min. HeLa cells were seeded on microscope cover glasses (Marienfeld, 0111520) at 10^5 cells/ml and left overnight for adhesion. Cells were then rinsed three times with PBS, and CPP-QD-Tb solutions were added. Cells were incubated for 3 hours at 37°C and 5% CO₂. After incubation, cells were washed three times with PBS and fixed with 4% paraformaldehyde in PBS for 10 min. Cells were rinsed twice with PBS and mounted onto glass slides with a drop of Fluoro-Gel (Electron Microscopy Sciences, 17985-10) mounting medium. For FRET efficiency control experiments that account for the Tb spectral crosstalk to the Tb-to-QD detection channel, A549 cells were incubated with a primary antibody against anti-E-cadherin and a secondary antibody labeled with Lumi4(Tb).

TG microscopy with laser excitation

Images of Tb-to-QD FRET experiments for cellular delivery with CPPs were acquired using a wide-field, TG luminescence inverted microscope (Olympus IX71) that uses a UV laser [349 nm, 100 Hz, Nd:YLF (neodymium-doped yttrium lithium fluoride), Triton, Spectra-Physics] for pulsed excitation and an ICCD camera (PI-MAX3, Princeton Instruments) for gated detection. Fluorescence signal was collected with a high-NA (=1.35) objective (UPLSAPO 60XO, Olympus) and was detected using two channels: a donor (Tb) channel with a 405-nm dichroic mirror (Di02-R405) and 542-nm band-pass filter (FF01-542/20-25) and an acceptor (Tb-to-QD FRET) channel with a 552-nm dichroic (FF552-Di02) and 605-nm (FF01-605/15-25) or 620-nm (FF01-620/14-25) band-pass filter. All filters were purchased from Semrock Inc. Acquisition settings in WinView software controlling the camera were generally fixed at the following: delay time, 10 μs (plus intensifier time, 870 ns); gate width, 2.5 ms; gates/exposure, 400 to 800; and intensifier gain, 100 V.

SS microscopy

SS microscopy was particularly used to observe the QD signals. QDs were excited through the epi-illuminator and 60× magnification objective (UPLSAPO 60XO, Olympus) system using a mercury lamp (X-Cite 120Q, Lumen Dynamics). The luminescence was collected using the same objective and a set of filters: 438-nm (FF02-438/24-25) or 494-nm (FF01-494/20-25) excitation filter, 552-nm dichroic mirror (FF552-Di02), and 605-nm (FF01-605/15-25) or 620-nm (FF01-620/14-25) emission filter. Images were recorded with a CMOS camera (pco.edge, PCO), with acquisition times below 30 ms.

SUPPLEMENTARY MATERIALS

Supplementary material for this article is available at <http://advances.sciencemag.org/cgi/content/full/2/6/e1600265/DC1>

fig. S1. PL images of A431 cells labeled with anti-EGFR-Tb and anti-HER2-QD antibody conjugates.

fig. S2. Intracellular Tb-to-QD FRET at 0.9 μM QD concentrations.

fig. S3. Calibration of microinjection system.

fig. S4. Cellular uptake of CPP-QDs at different QD concentrations.

fig. S5. Cellular uptake of QD at different CPP per QD valencies.

fig. S6. PL images of CPP₄₀-QD-Tb₄₀ nanoassemblies internalized into HeLa cells.

fig. S7. QD ligand structures.

REFERENCES AND NOTES

1. S. Mehta, J. Zhang, Reporting from the field: Genetically encoded fluorescent reporters uncover signaling dynamics in living biological systems, *Annu. Rev. Biochem.* **80**, 375–401 (2011).
2. C. M. Welch, H. Elliott, G. Danuser, K. M. Hahn, Imaging the coordination of multiple signalling activities in living cells. *Nat. Rev. Mol. Cell Biol.* **12**, 749–756 (2011).

3. A. Miyawaki, Development of probes for cellular functions using fluorescent proteins and fluorescence resonance energy transfer. *Annu. Rev. Biochem.* **80**, 357–373 (2011).
4. I. L. Medintz, N. Hildebrandt, *FRET—Förster Resonance Energy Transfer: From Theory to Applications* (Wiley-VCH Verlag GmbH and Co. KGaA, Weinheim, ed. 1, 2013).
5. C. Berney, G. Danuser, FRET or no FRET: A quantitative comparison. *Biophys. J.* **84**, 3992–4010 (2003).
6. D. W. Piston, G.-J. Kremers, Fluorescent protein FRET: The good, the bad and the ugly. *Trends Biochem. Sci.* **32**, 407–414 (2007).
7. E. Galperin, V. V. Verkhusha, A. Sorkin, Three-chromophore FRET microscopy to analyze multiprotein interactions in living cells. *Nat. Methods* **1**, 209–217 (2004).
8. D. M. Shcherbakova, M. A. Hink, L. Joosen, T. W. J. Gadella, V. V. Verkhusha, An orange fluorescent protein with a large Stokes shift for single-excitation multicolor FCCS and FRET imaging. *J. Am. Chem. Soc.* **134**, 7913–7923 (2012).
9. J. C. Bünzli, S. V. Eliseeva, in *Lanthanide Luminescence: Photophysical, Analytical and Biological Aspects*, P. Hanninen, H. Harma, Eds. (Springer-Verlag, Berlin, 2011), vol. 7, pp. 1–47.
10. J.-C. Bünzli, Lanthanide luminescence for biomedical analyses and imaging. *Chem. Rev.* **110**, 2729–2755 (2010).
11. N. Hildebrandt, K. D. Wegner, W. R. Algar, Luminescent terbium complexes: Superior Förster resonance energy transfer donors for flexible and sensitive multiplexed biosensing. *Coord. Chem. Rev.* **273–274**, 125–138 (2014).
12. M. Rajendran, E. Yapici, L. W. Miller, Lanthanide-based imaging of protein–protein interactions in live cells. *Inorg. Chem.* **53**, 1839–1853 (2014).
13. D. Geißler, N. Hildebrandt, Lanthanide complexes in FRET applications. *Curr. Inorg. Chem.* **1**, 17–35 (2011).
14. F. Degorce, A. Card, S. Soh, E. Trinquet, G. P. Knapik, B. Xie, HTRF: A technology tailored for drug discovery—A review of theoretical aspects and recent applications. *Curr. Chem. Genomics* **3**, 22–32 (2009).
15. D. Geißler, S. Stufler, H.-G. Löhmansröben, N. Hildebrandt, Six-color time-resolved Förster resonance energy transfer for ultrasensitive multiplexed biosensing. *J. Am. Chem. Soc.* **135**, 1102–1109 (2013).
16. A. Ho-Pun-Cheung, H. Bazin, N. Gaborit, C. Larbouret, P. Garnerio, E. Assenat, F. Castan, C. Bascoul-Mollevi, J. Ramos, M. Ychou, A. Pèlegri, G. Mathis, E. Lopez-Crapez, Quantification of HER expression and dimerization in patients' tumor samples using time-resolved Förster resonance energy transfer. *PLoS One* **7**, e37065 (2012).
17. H. E. Rajapakse, N. Gahlaut, S. Mohandessi, D. Yu, J. R. Turner, L. W. Miller, Time-resolved luminescence resonance energy transfer imaging of protein–protein interactions in living cells. *Proc. Natl. Acad. Sci. U.S.A.* **107**, 13582–13587 (2010).
18. D. Jin, J. A. Piper, Time-gated luminescence microscopy allowing direct visual inspection of lanthanide-stained microorganisms in background-free condition. *Anal. Chem.* **83**, 2294–2300 (2011).
19. M. Delbianco, V. Sadovnikova, E. Bourrier, G. Mathis, L. Lamarque, J. M. Zwier, D. Parker, Bright, highly water-soluble triazacyclononane europium complexes to detect ligand binding with time-resolved FRET microscopy. *Angew. Chem. Int. Ed.* **53**, 10718–10722 (2014).
20. O. Faklaris, M. Cottet, A. Falco, B. Villier, M. Laget, J. M. Zwier, E. Trinquet, B. Mouillac, J.-P. Pin, T. Durroux, Multicolor time-resolved Förster resonance energy transfer microscopy reveals the impact of GPCR oligomerization on internalization processes. *FASEB J.* **29**, 2235–2246 (2015).
21. S. Lindén, M. K. Singh, K. D. Wegner, M. Regairaz, F. Dautry, F. Treussart, N. Hildebrandt, Terbium-based time-gated Förster resonance energy transfer imaging for evaluating protein–protein interactions on cell membranes. *Dalton Trans.* **44**, 4994–5003 (2015).
22. N. Hildebrandt, L. J. Charbonniere, M. Beck, R. F. Ziessel, H.-G. Löhmansröben, Quantum dots as efficient energy acceptors in a time-resolved fluoroimmunoassay. *Angew. Chem. Int. Ed.* **44**, 7612–7615 (2005).
23. L. J. Charbonnière, N. Hildebrandt, R. F. Ziessel, H.-G. Löhmansröben, Lanthanides to quantum dots resonance energy transfer in time-resolved fluoro-immunoassays and luminescence microscopy. *J. Am. Chem. Soc.* **128**, 12800–12809 (2006).
24. D. Geißler, L. J. Charbonnière, R. F. Ziessel, N. G. Butlin, H.-G. Löhmansröben, N. Hildebrandt, Quantum dot biosensors for ultrasensitive multiplexed diagnostics. *Angew. Chem. Int. Ed.* **49**, 1396–1401 (2010).
25. L. J. Charbonnière, N. Hildebrandt, Lanthanide complexes and quantum dots: A bright wedding for resonance energy transfer. *Eur. J. Inorg. Chem.* **2008**, 3241–3251 (2008).
26. F. Morgner, D. Geißler, S. Stufler, N. G. Butlin, H.-G. Löhmansröben, N. Hildebrandt, A quantum-dot-based molecular ruler for multiplexed optical analysis. *Angew. Chem. Int. Ed.* **49**, 7570–7574 (2010).
27. W. R. Algar, D. Wegner, A. L. Huston, J. B. Blanco-Canosa, M. H. Stewart, A. Armstrong, P. E. Dawson, N. Hildebrandt, I. L. Medintz, Quantum dots as simultaneous acceptors and donors in time-gated Förster resonance energy transfer relays: Characterization and biosensing. *J. Am. Chem. Soc.* **134**, 1876–1891 (2012).
28. K. D. Wegner, Z. Jin, S. Lindén, T. L. Jennings, N. Hildebrandt, Quantum-dot-based Förster resonance energy transfer immunoassay for sensitive clinical diagnostics of low-volume serum samples. *ACS Nano* **7**, 7411–7419 (2013).

29. D. Geißler, S. Linden, K. Liermann, K. D. Wegner, L. J. Charbonnière, N. Hildebrandt, Lanthanides and quantum dots as Förster resonance energy transfer agents for diagnostics and cellular imaging. *Inorg. Chem.* **53**, 1824–1838 (2014).
30. X. Qiu, N. Hildebrandt, Rapid and multiplexed microRNA diagnostic assay using quantum dot-based Förster resonance energy transfer. *ACS Nano* **9**, 8449–8457 (2015).
31. K. E. Sapsford, D. Farrell, S. Sun, A. Rasooly, H. Mattoussi, I. L. Medintz, Monitoring of enzymatic proteolysis on a electroluminescent-CCD microchip platform using quantum dot-peptide substrates. *Sens. Actuators B* **139**, 13–21 (2009).
32. J. B. Blanco-Canosa, M. Wu, K. Susumu, E. Petryayeva, T. L. Jennings, P. E. Dawson, W. R. Algar, I. L. Medintz, Recent progress in the bioconjugation of quantum dots. *Coord. Chem. Rev.* **263–264**, 101–137 (2014).
33. J. Capdevila, E. Elez, T. Macarulla, F. J. Ramos, M. Ruiz-Echarri, J. Taberner, Anti-epidermal growth factor receptor monoclonal antibodies in cancer treatment. *Cancer Treat. Rev.* **35**, 354–363 (2009).
34. E. G. Hofman, M. O. Ruonala, A. N. Bader, D. van den Heuvel, J. Voortman, R. C. Roovers, A. J. Verkleij, H. C. Gerritsen, P. M. P. van Bergen en Henegouwen, EGF induces coalescence of different lipid rafts. *J. Cell Sci.* **121**, 2519–2528 (2008).
35. K. D. Wegner, S. Lindén, Z. Jin, T. L. Jennings, R. el Khoulati, P. M. P. van Bergen en Henegouwen, N. Hildebrandt, Nanobodies and nanocrystals: Highly sensitive quantum dot-based homogeneous FRET immunoassay for serum-based EGFR detection. *Small* **10**, 734–740 (2014).
36. K. Susumu, E. Oh, J. B. Delehanty, J. B. Blanco-Canosa, B. J. Johnson, V. Jain, W. J. Hervey IV, W. R. Algar, K. Boeneman, P. E. Dawson, I. L. Medintz, Multifunctional compact zwitterionic ligands for preparing robust biocompatible semiconductor quantum dots and gold nanoparticles. *J. Am. Chem. Soc.* **133**, 9480–9496 (2011).
37. K. Boeneman, J. B. Delehanty, J. B. Blanco-Canosa, K. Susumu, M. H. Stewart, E. Oh, A. L. Huston, G. Dawson, S. Ingale, R. Walters, M. Domowicz, J. R. Deschamps, W. R. Algar, S. Dimaggio, J. Manono, C. M. Spillmann, D. Thompson, T. L. Jennings, P. E. Dawson, I. L. Medintz, Selecting improved peptidyl motifs for cytosolic delivery of disparate protein and nanoparticle materials. *ACS Nano* **7**, 3778–3796 (2013).
38. R. Agarwal, M. S. Domowicz, N. B. Schwartz, J. Henry, I. Medintz, J. B. Delehanty, M. H. Stewart, K. Susumu, A. L. Huston, J. R. Deschamps, P. E. Dawson, V. Palomo, G. Dawson, Delivery and tracking of quantum dot peptide bioconjugates in an intact developing avian brain. *ACS Chem. Neurosci.* **6**, 494–504 (2015).
39. M. Rajendran, L. W. Miller, Evaluating the performance of time-gated live-cell microscopy with lanthanide probes. *Biophys. J.* **109**, 240–248 (2015).
40. G. H. Patterson, S. M. Knobel, W. D. Sharif, S. R. Kain, D. W. Piston, Use of the green fluorescent protein and its mutants in quantitative fluorescence microscopy. *Biophys. J.* **73**, 2782–2790 (1997).
41. W. R. Algar, A. P. Malanoski, K. Susumu, M. H. Stewart, N. Hildebrandt, I. L. Medintz, Multiplexed tracking of protease activity using a single color of quantum dot vector and a time-gated Förster resonance energy transfer relay. *Anal. Chem.* **84**, 10136–10146 (2012).
42. J. C. Claussen, W. R. Algar, N. Hildebrandt, K. Susumu, M. G. Ancona, I. L. Medintz, Biophotonic logic devices based on quantum dots and temporally-staggered Förster energy transfer relays. *Nanoscale* **5**, 12156–12170 (2013).
43. J. C. Claussen, N. Hildebrandt, K. Susumu, M. G. Ancona, I. L. Medintz, Complex logic functions implemented with quantum dot bionanophotonic circuits. *ACS Appl. Mater. Interfaces* **6**, 3771–3778 (2014).
44. B. C. Mei, K. Susumu, I. L. Medintz, J. B. Delehanty, T. J. Mountziaris, H. Mattoussi, Modular poly(ethylene glycol) ligands for biocompatible semiconductor and gold nanocrystals with extended pH and ionic stability. *J. Mater. Chem.* **18**, 4949–4958 (2008).
45. J. Breger, J. B. Delehanty, I. L. Medintz, Continuing progress toward controlled intracellular delivery of semiconductor quantum dots. *Wiley Interdiscip. Rev. Nanomed. Nanobiotechnol.* **7**, 131–151 (2015).
46. L. D. Field, J. B. Delehanty, Y. Chen, I. L. Medintz, Peptides for specifically targeting nanoparticles to cellular organelles: *Quo vadis?* *Acc. Chem. Res.* **48**, 1380–1390 (2015).
47. C. E. Bradburne, J. B. Delehanty, K. Boeneman Gemmill, B. C. Mei, H. Mattoussi, K. Susumu, J. B. Blanco-Canosa, P. E. Dawson, I. L. Medintz, Cytotoxicity of quantum dots used for in vitro cellular labeling: Role of QD surface ligand, delivery modality, cell type, and direct comparison to organic fluorophores. *Bioconjug. Chem.* **24**, 1570–1583 (2013).
48. B. D. Grant, J. G. Donaldson, Pathways and mechanisms of endocytic recycling. *Nat. Rev. Mol. Cell Biol.* **10**, 597–608 (2009).
49. K. Kantner, S. Ashraf, S. Carregal-Romero, C. Carrillo-Carrion, M. Collot, P. del Pino, W. Heimbrodt, D. Jimenez De Aberasturi, U. Kaiser, L. I. Kazakova, M. Lelle, N. Martinez de Baroja, J. M. Montenegro, M. Nazarenus, B. Pelaz, K. Peneva, P. R. Gil, N. Sabir, L. M. Schneider, L. I. Shabarchina, G. B. Sukhorukov, M. Vazquez, F. Yang, W. J. Parak, Particle-based optical sensing of intracellular ions at the example of calcium—What are the experimental pitfalls? *Small* **11**, 896–904 (2015).
50. Y.-Q. Wang, C. Ye, Z.-H. Zhu, Y.-Z. Hu, Cadmium telluride quantum dots as pH-sensitive probes for tiopronin determination. *Anal. Chim. Acta* **610**, 50–56 (2008).
51. R. P. Haugland, Ed., *The Handbook: A Guide to Fluorescent Probes and Labeling Technologies* (Invitrogen, San Diego, CA, ed. 10, 2005), p. 1126.
52. W. G. Kreyling, A. M. Abdelmonem, Z. Ali, F. Alves, M. Geiser, N. Haberl, R. Hartmann, S. Hirn, D. Jimenez de Aberasturi, K. Kantner, G. Khadem-Saba, J.-M. Montenegro, J. Rejman, T. Rojo, I. Ruiz de Larramendi, R. Ufartes, A. Wenk, W. J. Parak, In vivo integrity of polymer-coated gold nanoparticles. *Nat. Nanotechnol.* **10**, 619–623 (2015).
53. J. D. Xu, T. M. Cornieille, E. G. Moore, G.-L. Law, N. G. Butler, K. N. Raymond, Octadentate cages of Tb(III) 2-hydroxyisophthalamides: A new standard for luminescent lanthanide labels. *J. Am. Chem. Soc.* **133**, 19900–19910 (2011).
54. D. E. Prasuhn, J. R. Deschamps, K. Susumu, M. H. Stewart, K. Boeneman, J. B. Blanco-Canosa, P. E. Dawson, I. L. Medintz, Polyvalent display and packing of peptides and proteins on semiconductor quantum dots: Predicted versus experimental results. *Small* **6**, 555–564 (2010).
55. J. C. Breger, M. G. Ancona, S. A. Walper, E. Oh, K. Susumu, M. H. Stewart, J. R. Deschamps, I. L. Medintz, Understanding how nanoparticle attachment enhances phosphotriesterase kinetic efficiency. *ACS Nano* **9**, 8491–8503 (2015).
56. J. B. Delehanty, C. E. Bradburne, K. Boeneman, K. Susumu, D. Farrell, B. C. Mei, J. B. Blanco-Canosa, G. Dawson, P. E. Dawson, H. Mattoussi, I. L. Medintz, Delivering quantum dot-peptide bioconjugates to the cellular cytosol: Escaping from the endolysosomal system. *Integr. Biol.* **2**, 265–277 (2010).
57. R. C. Roovers, T. Laeremans, L. Huang, S. De Taeye, A. J. Verkleij, H. Revets, H. J. de Haard, P. M. P. van Bergen en Henegouwen, Efficient inhibition of EGFR signalling and of tumour growth by antagonistic anti-EGFR Nanobodies. *Cancer Immunol. Immunother.* **56**, 303–317 (2007).
58. N. Gahlaut, L. W. Miller, Time-resolved microscopy for imaging lanthanide luminescence in living cells. *Cytometry A* **77A**, 1113–1125 (2010).
59. D. Jin, Y. Lu, R. C. Leif, S. Yang, M. Rajendran, L. W. Miller, Unit 2.22 how to build a time-gated luminescence microscope. *Curr. Protoc. Cytom.* **67**, 2.22.1–2.22.36 (2014).
60. C. A. Schneider, W. S. Rasband, K. W. Eliceiri, NIH Image to ImageJ: 25 years of image analysis. *Nat. Methods* **9**, 671–675 (2012).

Acknowledgments: We thank Lumiphore Inc. for the gift of Lumi4-Tb reagents and Merck KGaA for the gift of matuzumab antibodies. **Funding:** We thank the European Union (Innovative Medicines Initiative project OncoTrack), the French “Investment for the Future” program managed by Agence Nationale de la Recherche (grants “NanoCTC” ANR-10-Nano-05 and “Labex NanoSaclay” ANR-10-LABX-0035), and the U.S. NIH (grant R01 GM081030) for financial support. X.Q. acknowledges the China Scholarship Council for funding her Ph.D. fellowship. I.L.M. acknowledges the Defense Threat Reduction Agency and the Naval Research Laboratory Nanosience Institute. N.H. acknowledges the Institut Universitaire de France. **Author contributions:** L.W.M., N.H., and I.L.M. designed the study, analyzed the data, and wrote the manuscript. H.S.A., M.C.D.S., S.L., and T.C. performed microscopy experiments. M.C.D.S. analyzed the data and wrote the manuscript. X.Q. performed bioconjugation experiments. P.M.P.v.B.e.H. produced single-domain antibodies. T.L.J. and K.S. produced QDs. **Competing interests:** The authors declare that they have no competing interests. **Data and materials availability:** All data needed to evaluate the conclusions in the paper are present in the paper and/or the Supplementary Materials. Additional data related to this paper may be requested from the authors.

Submitted 9 February 2016

Accepted 19 May 2016

Published 10 June 2016

10.1126/sciadv.1600265

Citation: H. S. Afsari, M. Cardoso dos Santos, S. Lindén, T. Chen, X. Qiu, P. M. P. van Bergen en Henegouwen, T. L. Jennings, K. Susumu, I. L. Medintz, N. Hildebrandt, L. W. Miller, Time-gated FRET nanoassemblies for rapid and sensitive intra- and extracellular fluorescence imaging. *Sci. Adv.* **2**, e1600265 (2016).